Protein nanocages that penetrate airway mucus and tumor tissue

Xinglu Huang[a,b], Jane Chisholm[a,c], Jie Zhuang[d], Yanyu Xiao[a,e], Gregg Duncan[a,b], Xiaoyuan Chen[f], Jung Soo Suk[a,b,1], and Justin Hanes[a,b,c,g,1]

[a]Center for Nanomedicine, Wilmer Eye Institute, Johns Hopkins University School of Medicine, Baltimore, MD 21231; [b]Department of Ophthalmology, Wilmer Eye Institute, Johns Hopkins University School of Medicine, Baltimore, MD 21231; [c]Department of Chemical & Biomolecular Engineering, Johns Hopkins University, Baltimore, MD 21218; [d]Center for Molecular Medicine, National Heart, Lung, and Blood Institute, National Institutes of Health, Bethesda, MD 20892; [e]Department of Pharmaceutics, China Pharmaceutical University, Nanjing, Jiangsu 210009, China; [f]Laboratory of Molecular Imaging and Nanomedicine, National Institute of Biomedical Imaging and Bioengineering, National Institutes of Health, Bethesda, MD 20892; and [g]Department of Biomedical Engineering, Johns Hopkins University School of Medicine, Baltimore, MD 21205

Reports on drug delivery systems capable of overcoming multiple biological barriers are rare. We introduce a nanoparticle-based drug delivery technology capable of rapidly penetrating both lung tumor tissue and the mucus layer that protects airway tissues from nanoscale objects. Specifically, human ferritin heavy-chain nanocages (FTn) were functionalized with polyethylene glycol (PEG) in a unique manner that allows robust control over PEG location (nanoparticle surface only) and surface density. We varied PEG surface density and molecular weight to discover PEGylated FTn that rapidly penetrated both mucus barriers and tumor tissues in vitro and in vivo. Upon inhalation in mice, PEGylated FTn with optimized PEGylation rapidly penetrated the mucus gel layer and thus provided a uniform distribution throughout the airways. Subsequently, PEGylated FTn preferentially penetrated and distributed within orthotopic lung tumor tissue, and selectively entered cancer cells, in a transferrin receptor 1-dependent manner, which is up-regulated in most cancers. To test the potential therapeutic benefits, doxorubicin (DOX) was conjugated to PEGylated FTn via an acid-labile linker to facilitate intracellular release of DOX after cell entry. Inhalation of DOX-loaded PEGylated FTn led to 60% survival, compared with 10% survival in the group that inhaled DOX in solution at the maximally tolerated dose, in a murine model of malignant airway lung cancer. This approach may provide benefits as an adjuvant therapy combined with systemic chemo- or immunotherapy or as a stand-alone therapy for patients with tumors confined to the airways.

lung cancer | nanoparticle | biological barriers | PEG | human ferritin

A myriad of nanoparticle-based drug delivery systems have been introduced on a daily basis over the past few decades, however only a few have reached the clinic with marginal benefits achieved at best (1). This is most likely attributed to the difficulty in designing a simple delivery system capable of simultaneously addressing multiple biological barriers. The odds of translating complex multifunctional systems into the clinic are dismally low, as it is highly challenging to formulate them in a reproducible and scalable manner. Here, we report a proof-of-concept nanoparticle-based platform that is safe, simple, and overcomes multiple biological barriers. Specifically, we endowed human protein-based nanocages, possessing an intrinsic ability to preferentially target cancer cells, with surfaces that resist nonspecific interactions in physiological environments. We then evaluated their ability to breach through different delivery barriers in vitro, ex vivo, and in vivo and investigated their potential in treating tumors at a mucosal surface, specifically in an orthotopic airway cancer model.

Ferritin is the primary iron transport and storage protein in both prokaryotes and eukaryotes and is composed of 24 subunits of the ferritin heavy and light chains each (2). Thus, the human ferritin protein is nonimmunogenic and likely to be safe for medical applications. Unlike the naturally occurring ferritin

protein, self-assembled ferritin nanocages (FTn) are engineered with only the 24 ferritin heavy chains into structures that possess an internal cavity that can accommodate therapeutic and/or diagnostic agents (3). FTn possess a diameter of 12 nm (4), which is smaller than that required to facilitate delivery of payloads through nanoporous tissue barriers, including interstitial tissues (5) and poorly permeable tumors (6). More importantly, its intrinsic and selective affinity to the transferrin receptor 1 (TfR 1) (7, 8), which is highly expressed on rapidly dividing tumor cells (9), renders FTn an attractive drug delivery platform to treat cancer. Indeed, FTn have been explored as a means to improve systemic delivery of various drugs for cancer treatment (10–12). However, systemic delivery of FTn-based formulations may cause undesired side effects, as TfR 1 is highly expressed on many cell types in systemic circulation, including erythroid precursors (13) and activated lymphocytes (14). We rationalized that inhaled delivery of FTn-based chemotherapeutics may provide a novel approach for the treatment of lung cancer, especially those that are confined to the airways.

One of the primary barriers to effective inhalation of therapeutics to the lung airways is the protective mucus gel layer lining the airway epithelium (15, 16). The airway mucus gel is a dense network of highly adhesive macromolecules (16, 17) that traps

Significance

In designing new nanoparticle drug delivery systems, it is critical to identify simple formulations that overcome multiple biological barriers while being safe, reproducible, and scalable. We modified human ferritin nanocages using a unique PEGylation strategy, which provides a highly uniform, stable, and compact nanocarrier platform capable of overcoming multiple biological barriers, specifically penetration of airway mucus and tumor tissue, selective uptake by cancer cells, and drug release triggered only upon cell uptake. Surprisingly, PEGylation of ferritin to overcome the mucus barrier did not interfere with the ability of the nanocages to form particles, penetrate tumor tissues, and enter cells. Proof-of-concept of the system is provided in the treatment of an aggressive orthotopic model of lung cancer.
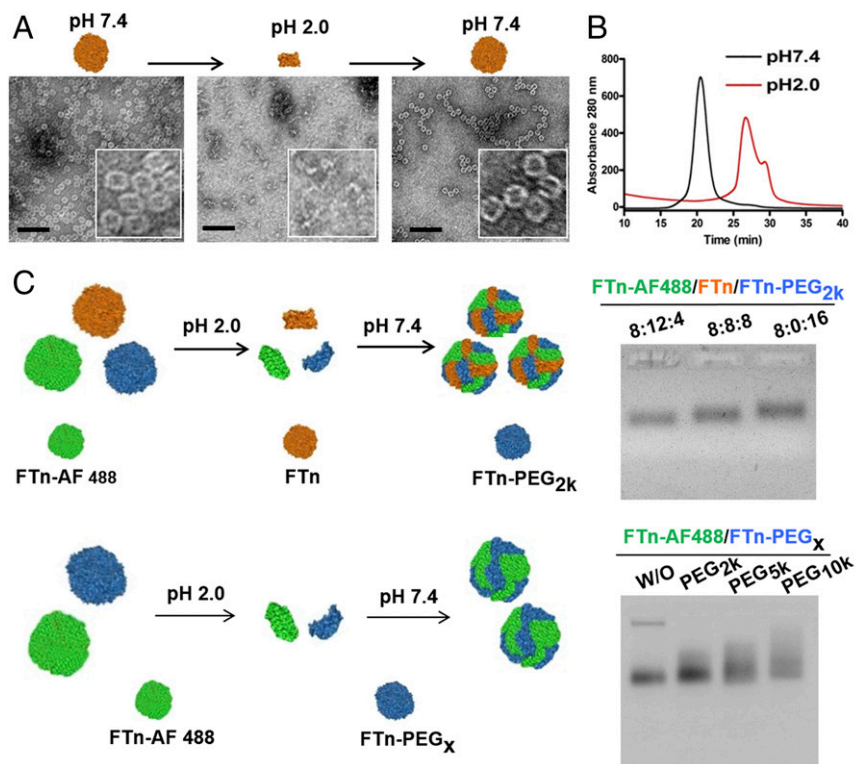
Fig. 1. Physicochemical characterization of FTn. (*A*) TEM images of nanostructures of FTn at pH 7.4 and pH 2.0 (stained with 1% uranyl acetate). (Scale bars, 50 nm.) (*B*) The diameters of FTn at pH 7.4 and pH 2.0 were analyzed by size chromatography. (*C*) Surface modification does not affect reassembly capacity of FTn. FTn with different modification were reassembled by controlling pH. (*Top*) Gel electrophoresis of the reassembled FTn formulated with varying ratios of FTn to FTn–PEG$_{2k}$ (the ratio of AF488-labeled FTn used was fixed; 8 of 24 subunits). (*Bottom*) Gel electrophoresis analysis of the reassembled particles with AF488-labeled FTn and non-PEGylated/PEGylated FTn (PEG molecular mass = 2, 5, and 10 kDa) (the ratio of AF488-labeled FTn used was fixed).

most inhaled particulate matter, including therapeutic nanoparticles, leading to their rapid elimination from the lungs by mucociliary clearance (MCC) (18). To avoid trapping in the mucus gel, nanoparticles can be coated with a dense corona of polyethylene glycol (PEG) (19–23). However, PEGylation may interfere with the intrinsic ability of FTn to target cancers via TfR 1. The effect of PEGylation on the native functionality of protein-based therapeutics is strongly dependent upon the molecular weight (MW) of the conjugated PEG (24–26). Based on these findings, we hypothesized that the use of low-MW PEG to coat FTn may allow the particles to not only rapidly penetrate the mucus gel layer but also retain their cancer-targeting properties. To test this hypothesis, we prepared various formulations of FTn, each coated with a different MW of PEG, using a unique strategy to incorporate a controlled density of PEG exclusively on the particle surface. The candidate formulations were studied for the impact of PEG MW on the ability of the PEGylated FTn to simultaneously overcome the critical biological barriers to inhaled nanoparticle-based chemotherapy in vivo. Based on these results, we designed a chemotherapeutic loaded PEGylated FTn where doxorubicin (DOX) was conjugated to the PEGylated FTn via an acid-sensitive linker, thereby providing a high drug loading and drug release triggered by cell uptake and subsequent sequestration in acidic vesicles. Finally, we investigated the efficacy of DOX-loaded PEGylated FTn in an orthotopic model of aggressive lung cancer.

Results

PEGylated FTn with Controlled PEG Location and Surface Density. We genetically engineered recombinant FTn by transforming bacterial cells with a custom-made plasmid encoding for human native ferritin heavy chain. Subsequently, purified FTn were confirmed

to undergo controlled cage dissociation under acidic conditions and reassembly at neutral pH, via their intrinsic pH-dependent property (3). Transmission electron microscopy (TEM) revealed that FTn existed as monodispersed nanocages at pH 7.4, dissociated to individual subunits at pH 2, and then reassembled to form nanocages when the pH was returned to 7.4 (Fig. 1*A*). The diameter of FTn at different pH was measured by size exclusion chromatography (Fig. S1), yielding a single peak at the size of 13.2 nm at pH 7.4 and a broad peak with a size range of 1.8–5.4 nm at pH 2.0 (Fig. 1*B*).

We next conjugated PEG to intact FTn at neutral pH to attach PEG selectively to the primary amines exposed on the outer surface of FTn. Because 336 primary amines are present in each FTn based on sequence analysis, we first conjugated 2 kDa PEG (PEG$_{2k}$) to FTn at a molar ratio of 500:1, and the surface PEG density was fluorometrically determined (16) to be ~0.4 PEG per square nanometer, which corresponds to ~190 PEG per FTn. Likewise, 5 and 10 kDa PEG (PEG$_{5k}$ and PEG$_{10k}$, respectively) were conjugated to separate aliquots of FTn. All PEGylated FTn exhibited cage-like structures (Fig. S2*A*) that appeared similar to FTn before PEGylation. In parallel, Alexa Fluor 488 (AF488) and Cy5 molecules were conjugated to FTn for gel electrophoretic and microscopic visualization of FTn, respectively. Subsequently, different FTn formulations, including non-PEGylated FTn, fluorescently labeled FTn (either AF488- or Cy5-labeled FTn), and FTn–PEG$_x$ (x = 2, 5, or 10 kDa), were disassembled at pH 2 and reassembled at various blending ratios to yield hybrid FTn. This unique PEGylation strategy ensures that all PEG molecules are conjugated only at the surface of FTn while providing a highly controlled surface density of PEG. We confirmed with TEM that the blending process did not disrupt the formation of cage-like hybrid FTn (Fig. S2*B*). Using gel electrophoresis, we next found that increasing the fraction of PEGylated
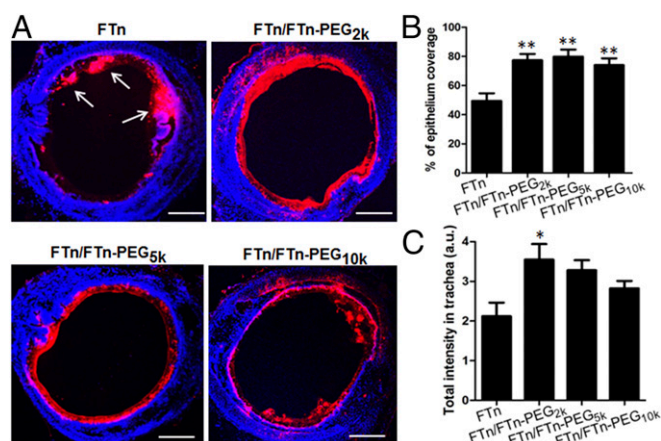
Fig. 2. Distribution of FTn/FTn–PEG$_x$ throughout the mucus-covered mouse lung airways. (*A*) Representative images of the in vivo distribution of Cy5-labeled FTn or FTn/FTn–PEG$_x$ (x = 2, 5, and 10 kDa) (red) in the large airways of mice (*n* = 4 mice). Cell nuclei are stained with DAPI (blue). (Scale bars, 200 μm.) (*B*) Image-based quantification of the coverage area of various particles in the large airways. Tissues were harvested 10 min after intratracheal administration. Data represent mean percentage coverage ± SEM. **$P < 0.01$ compared with the non-PEGylated FTn. (*C*) Image-based quantification of the total fluorescence intensity distributed throughout mouse airways. *$P < 0.05$ compared with the non-PEGylated FTn.

FTn in the hybrid FTn, or increasing the MW of PEG used to create hybrid FTn, decreased the running rates on the agarose gels (Fig. 1*C*), thus providing evidence that the overall MW of the PEGylated FTn increased in each case as expected. To minimally affect the intrinsic targeting ability of FTn, subsequent studies were conducted with hybrid FTn reassembled at a 1:1 ratio of FTn and FTn–PEG$_x$ (FTn/FTn–PEG$_x$), unless otherwise stated. Theoretically, 50% inclusion of FTn–PEG$_x$ should result in the surface PEG density of ~0.2 PEG per square nanometer, a PEG density that is expected to

lead to a brush-like conformation of PEG (27). Using fluorescently labeled PEG, we determined that the PEG surface density of hybrid FTn/FTn–PEG$_{2k}$ was ~0.24 ± 0.03 PEG per square nanometer.

In Vivo Airway Distribution of PEGylated FTn. We have previously demonstrated that muco-inert nanoparticles capable of efficiently penetrating airway mucus provide widespread in vivo distribution throughout the mouse airways following inhalation, whereas muco-adhesive nanoparticles were unable to do so (28, 29). We thus investigated the airway distribution of Cy5-labeled FTn, with or without PEG surface coatings, following intranasal administration in mice. We found that non-PEGylated FTn were aggregated in the mucus gel layer and, thus, sparsely distributed in airways (Fig. 2*A*). In contrast, PEGylated FTn, regardless of PEG MW, exhibited uniform and widespread distribution throughout the mouse airways (Fig. 2*A* and Fig. S3). Quantitatively, FTn/FTn–PEG$_{2k}$, FTn/FTn–PEG$_{5k}$, and FTn/FTn–PEG$_{10k}$ covered 77 ± 8, 80 ± 8, and 74 ± 8% of the mouse tracheal surfaces, respectively, compared with only 50 ± 9% by non-PEGylated FTn ($P < 0.01$) (Fig. 2*B*). We also found that FTn/FTn–PEG$_{2k}$ were retained at higher levels in the upper airway (i.e., trachea) 10 min after intratracheal administration compared with non-PEGylated FTn, as determined by quantifying the overall fluorescence intensity (Fig. 2*C*).

Tumor Cell Uptake, Tumor Tissue Penetration, and Safety of PEGylated FTn. We next sought to test whether PEGylated FTn were capable of cancer cell targeting in vitro. We first determined that Cy5-labeled FTn were taken up by mouse Lewis lung carcinoma (3LL) cells efficiently and in a dose-dependent manner (Fig. 3 *A* and *B*). FTn–Cy5 uptake was mediated by specific interactions between FTn and TfR 1, as confirmed by the significantly reduced binding observed in the presence of anti-TfR 1 antibody (Ab) (Fig. 3*C*). We also found that FTn were taken up by another TfR 1-positive human lung cancer cell line, A549, by the same mechanism (Fig. 3*C*). We then compared cell uptake of PEGylated and non-PEGylated FTn using flow cytometry. We found that the uptake
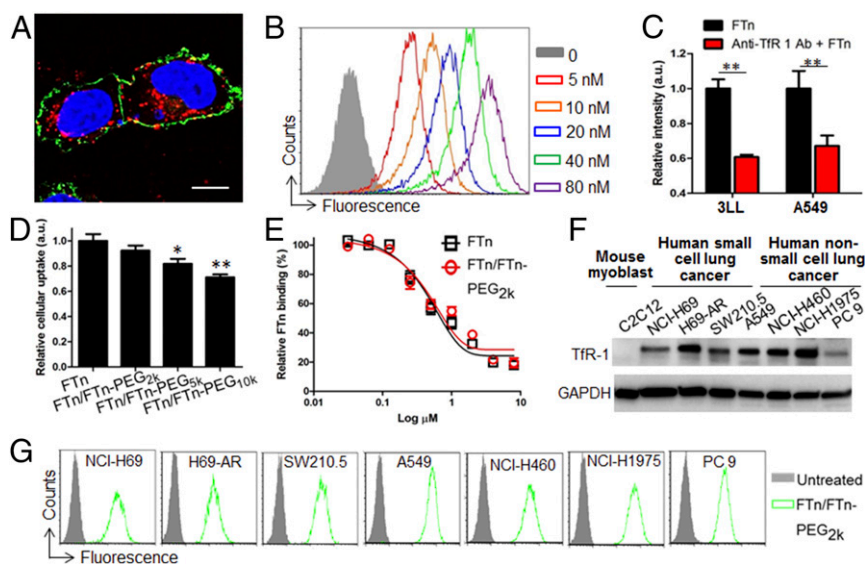

Fig. 3. Specific cell uptake and effect of PEGylation on the intrinsic cancer cell targeting capacity of FTn. (*A*) Confocal images of 3LL cells following incubation with the FTn. Blue, nucleus; green, membrane; red, Cy5-labeled FTn. (Scale bar, 20 μm.) (*B*) Flow cytometry analysis of cell uptake of Cy5-labeled FTn at different concentrations 2 h after the treatment. (*C*) Flow cytometry analysis of TfR 1-dependent cell binding of Cy5-labeled FTn to 3LL or A549 cells in the presence of anti-TfR 1 Ab. **$P < 0.01$. (*D*) Effect of PEG MW on the cell uptake of PEGylated FTn. *$P < 0.05$, **$P < 0.01$ compared with non-PEGylated FTn. (*E*) Competition binding of Cy5-labeled FTn to 3LL cells at different concentrations of FTn or FTn/FTn–PEG$_{2k}$. (*F*) Western blot analysis of TfR 1 expression in human NSCLC and SCLC cell lines as well as C2C12 normal cell line. (*G*) Flow cytometry analysis of the cell uptake of Cy5-labeled FTn/FTn–PEG$_{2k}$ in various lung cancer cell lines.
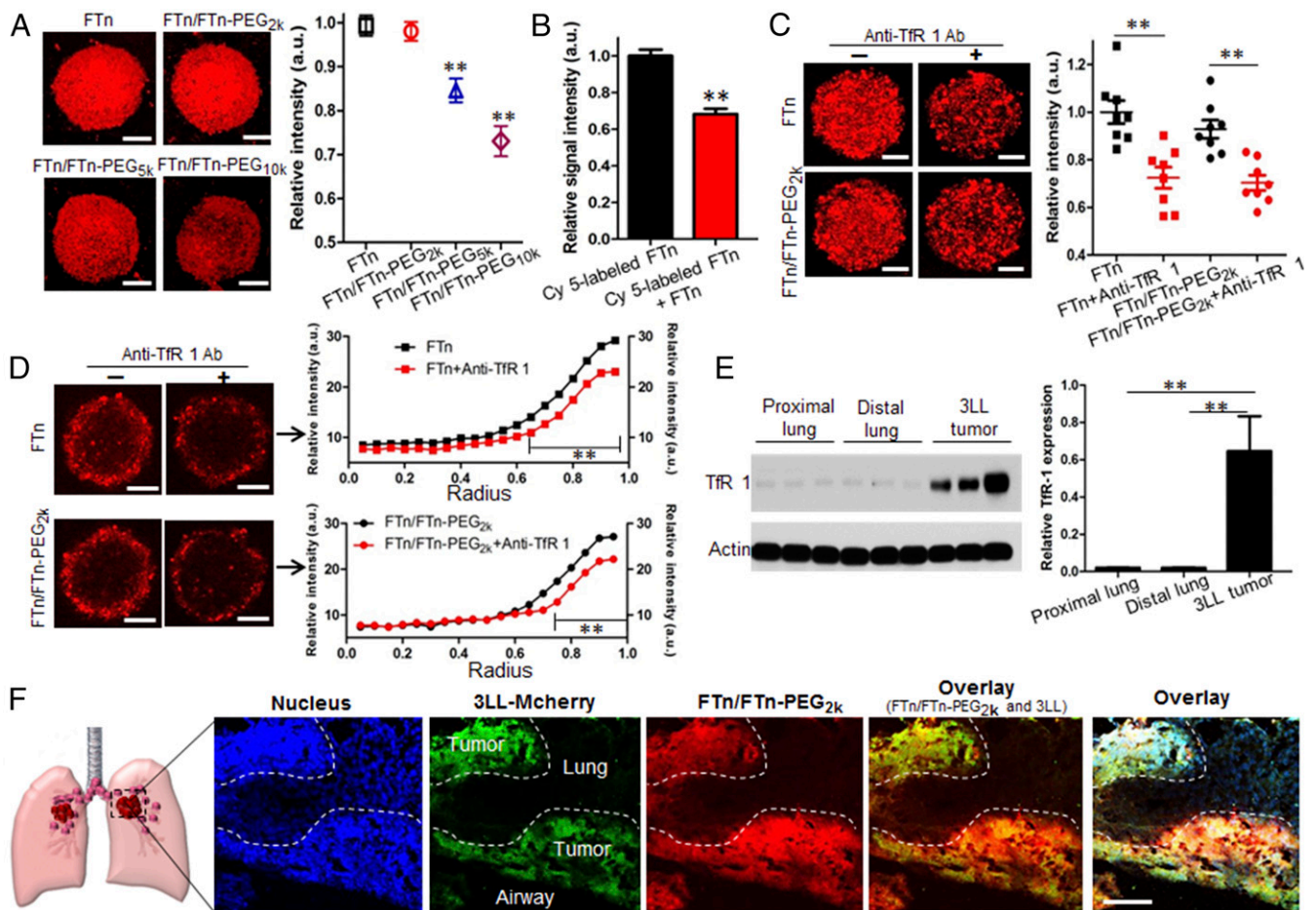
Huang et al.

Fig. 4. Deep penetration of PEGylated FTn throughout tumor tissues. (*A*) Effect of PEGylation on the penetration of FTn through a 3D tumor spheroid model established with 3LL cells. (*Left*) Representative confocal images of tumor penetration of the various particles in 3D spheroids. (Scale bar, 200 μm.) (*Right*) Image-based quantification of mean Cy5 fluorescence signal intensity in whole 3D-constructed cell spheroids. Data represent the average of $n \geq 8$ cell spheroids ($\pm$SEM). **$P < 0.01$ compared with non-PEGylated FTn. (*B*) Quantification analysis of tumor penetration of Cy5-labeled FTn in reconstructed 3D cell spheroids in the absence or presence of excess amounts of unlabeled FTn. **$P < 0.01$. (*C*) The penetration of the FTn and FTn/FTn–PEG$_{2k}$ through cell spheroids in the absence or presence of a 10-fold molar excess of anti-TfR 1 Ab. (Scale bar, 200 μm.) (*D*) Distribution of the Cy5 fluorescence signal in the middle section images of *C*. (*Left*) Representative middle section image. (*Right*) Image-based quantification of the mean intensity at different penetration distance (*Top*, FTn; *Bottom*, FTn/FTn–PEG$_{2k}$). Radius, 0 and 1 indicate the center and edge of the tumor spheroid, respectively. **$P < 0.01$ compared with FTn or FTn/FTn–PEG$_{2k}$. (Scale bar, 200 μm.) (*E*) Western blot analysis of TfR 1 expression in proximal and distal lung as well as 3LL tumor tissues. The tissues were collected from $n = 3$ mice for each group. **$P < 0.01$. (*F*) Colocalization (yellow) of intratracheally administered FTn/FTn–PEG$_{2k}$ (red) with an orthotopic 3LL lung cancer (mCherry; green). Cell nuclei are stained with DAPI (blue). (Scale bar, 100 μm.)

of PEGylated FTn with higher PEG MW, specifically FTn/FTn–PEG$_{5k}$ ($P < 0.05$) and FTn/FTn–PEG$_{10k}$ ($P < 0.01$), was significantly reduced compared with that of FTn; in contrast, the difference in the uptake of FTn and FTn/FTn–PEG$_{2k}$ was not statistically significant (Fig. 3*D*). A competitive binding analysis also revealed that FTn and FTn/FTn–PEG$_{2k}$ bound to 3LL cells to a similar extent (Fig. 3*E*). Additionally, FTn/FTn–PEG$_{2k}$ were efficiently taken up by several TfR 1-positive lung cancer cells, including both human small cell lung cancer (SCLC) and non-SCLC (NSCLC) cell lines (Fig. 3 *F* and *G*).

We next explored the effect of PEGylation on the penetration of Cy5-labeled FTn through a 3D tumor spheroid model established with 3LL cells. The multicellular tumor spheroids constitute the most commonly used in vitro model that recapitulates in vivo tumor microenvironments, as characterized by the presence of naturally formed extracellular matrix (ECM), regions of hypoxia and necrosis, and concentration gradients of oxygen and nutrients (30–32). The 3D-reconstructed confocal images of spheroids revealed that FTn and FTn/FTn–PEG$_{2k}$ uniformly distributed throughout the entire spheroids including the core (Fig. 4*A*, *Left*).

In contrast, FTn/FTn–PEG$_{5k}$ and FTn/FTn–PEG$_{10k}$ were found primarily near the periphery of tumor spheroids (Fig. 4*A*, *Left*). The mean fluorescence signal intensity within the tumor spheroids was indistinguishable between FTn and FTn/FTn–PEG$_{2k}$, whereas the FTn/FTn–PEG$_{5k}$ and FTn/FTn–PEG$_{10k}$ exhibited significantly lower intensity compared with FTn ($P < 0.01$) (Fig. 4*A*, *Right*).

To understand the mechanism of tumor penetration, we investigated the penetration of FTn and FTn/FTn–PEG$_{2k}$ in the presence of unlabeled FTn or anti-TfR 1 Ab. The penetration of Cy5-labeled FTn through the 3D tumor spheroids was significantly reduced in the presence of an excess amount of unlabeled FTn ($P < 0.01$) (Fig. 4*B*). The mean fluorescence signal intensities of FTn and FTn/FTn–PEG$_{2k}$ in the 3D-constructed tumor spheroids also significantly decreased in the presence of anti-TfR 1 Ab ($P < 0.01$) (Fig. 4*C*). The TfR 1-dependent tumor penetration was further confirmed by significantly reduced 2D penetration of both FTn and FTn/FTn–PEG$_{2k}$ from the surface toward the center of middle sections of the tumor spheroids (Fig. 4*D*).
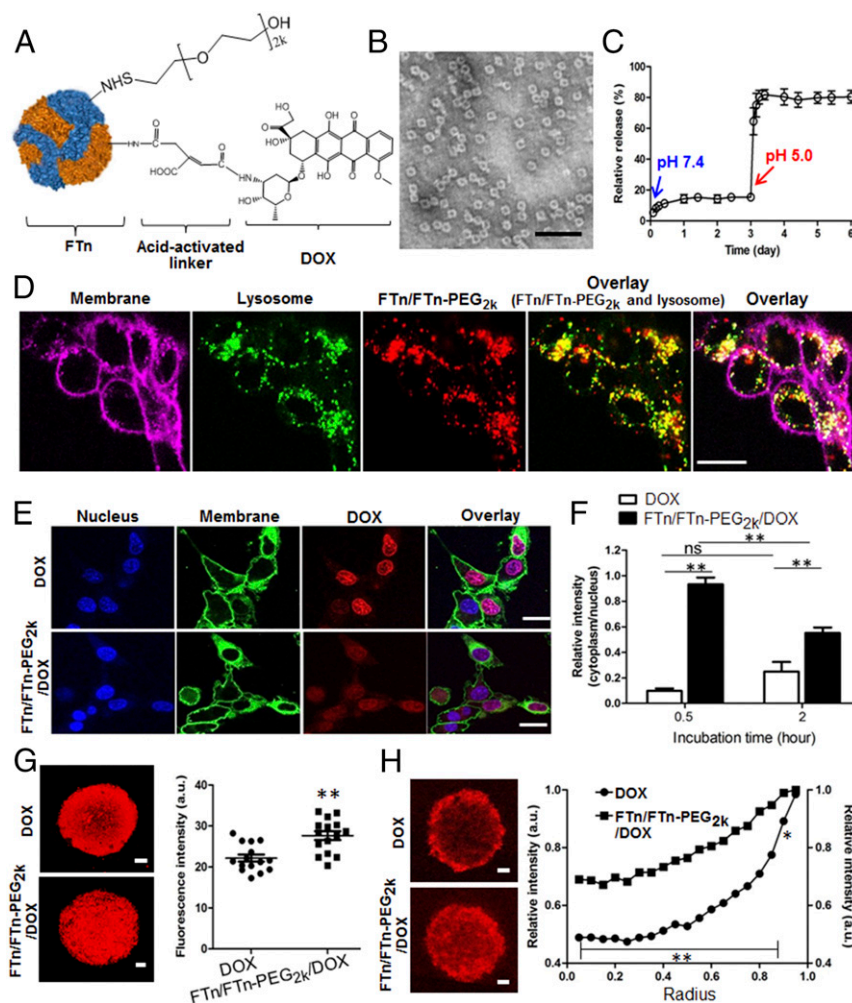
Fig. 5. Intracellular drug release and cell uptake of FTn/FTn–PEG$_{2k}$/DOX conjugates. (*A*) Schematic illustration of FTn/FTn–PEG$_{2k}$ conjugated with DOX via an acid-sensitive linker. (*B*) Representative TEM image of FTn/FTn–PEG$_{2k}$/DOX. (Scale bar, 100 nm.) (*C*) DOX release kinetics from FTn/FTn–PEG$_{2k}$/DOX incubated at pH 7.4 and pH 5.0. (*D*) Representative confocal images of the colocalization (yellow) of the Cy5-labeled FTn/FTn–PEG$_{2k}$ (red) and lysosome (green) in 3LL cells. (Scale bar, 10 μm.) (*E*) Representative confocal images of the cellular localization of free DOX (red) and FTn/FTn–PEG$_{2k}$/DOX (red) in 3LL cells. Cell membrane and nuclei are stained with Vybrant DiO (green) and DAPI (blue), respectively. (Scale bar, 10 μm.) (*F*) Relative amounts of free DOX or FTn/FTn–PEG$_{2k}$/DOX in cytoplasm over nuclei at different time points. ns, nonsignificant; **$P < 0.01$. (*G*) Tumor penetration of free DOX and FTn/FTn–PEG$_{2k}$/DOX in 3LL-based spheroids. (*Left*) Representative 3D reconstructed confocal images. (*Right*) Image-based quantification of the mean fluorescence intensity throughout the entire 3D reconstructed spheroids. **$P < 0.01$ compared with the free DOX. (Scale bars, 100 μm.) (*H*) Distribution of the DOX fluorescence signal in the middle section of spheroids. (*Left*) Representative middle section image. (*Right*) Image-based quantification of the mean intensity at different penetration distance. *$P < 0.05$, **$P < 0.01$ compared with the free DOX. (Scale bars, 100 μm.)

Based on the findings of the aforementioned studies, we identified FTn/FTn–PEG$_{2k}$ as the nanoparticle system that provides both efficient penetration through airway mucus and efficient tumor spheroid penetration in vitro. We next sought to investigate the behavior of FTn/FTn–PEG$_{2k}$ in vivo. To do this, we first determined that the TfR 1 expression in a 3LL-based s.c. tumor was over 30-fold higher ($P < 0.01$) than TfR 1 expression in healthy proximal and distal lung tissues (Fig. 4*E*). Subsequently, we developed an orthotopic mouse model of lung cancer by intratracheal inoculation of 3LL cells that constitutively express a fluorescent protein, mCherry, into the lungs of C57BL/6 mice. The orthotopic tumors were established along the airways and infiltrated into the healthy lung parenchyma 10 d after the inoculation (Fig. 4*F*). Cy5-labeled FTn/FTn–PEG$_{2k}$ that were intratracheally administered at this time were found preferentially within the mCherry-expressing tumor tissue (Fig. 4*F*). We also confirmed that lungs of healthy C57BL/6 mice intratracheally treated with an excess of FTn/FTn–PEG$_{2k}$ were virtually identical to untreated

lungs, without any apparent sign of acute cytotoxicity or inflammatory response (Fig. S4).

Formulation of DOX-Loaded FTn/FTn–PEG$_{2k}$. We next sought to attach a chemotherapeutic drug widely used for airway-related lung cancer therapy, DOX, to FTn/FTn–PEG$_{2k}$ in a manner that would limit its release primarily to tumor cells. To do so, we chemically conjugated DOX to FTn/FTn–PEG$_{2k}$ (hereafter, FTn/FTn–PEG$_{2k}$/DOX) via an acid-sensitive linker to achieve high drug loading while limiting drug release to acidic environments, such as in intracellular endo-lysosomal vesicles (Fig. 5*A* and Fig. S5). Physicochemical properties, including hydrodynamic diameter (HD), surface charge (as indicated by ζ-potential), and morphology of FTn/FTn–PEG$_{2k}$/DOX, were comparable to those of FTn/FTn–PEG$_{2k}$ without DOX (Fig. 5*B* and Table S1). The number of DOX molecules conjugated to each FTn/FTn–PEG$_{2k}$ was 88 ± 5.

The pH-dependent release kinetics of DOX was evaluated by incubating FTn/FTn–PEG$_{2k}$/DOX in aqueous solutions of varying pH at 37 °C. The amount of DOX released over 3 d at pH 7.4 was

Huang et al.

www.manaraa.com

negligible. However, a burst release of DOX was observed upon lowering the pH to 5.0, reaching a maximum release of nearly 80% after 4 h (Fig. 5C). To visualize the intracellular trafficking, 3LL cells were incubated with Cy5-labeled FTn/FTn–PEG$_{2k}$ and lysosomes were stained with LysoTracker. Confocal images showed that FTn/FTn–PEG$_{2k}$ colocalized with lysosomes 2 h after the addition to cells (Fig. 5D). We also confirm that DOX-loaded FTn/FTn–PEG$_{2k}$ (i.e., FTn/FTn–PEG$_{2k}$/DOX) colocalized with lysosomes labeled with anti-LAMP 1 Ab at the same incubation time (Fig. S6). We next explored the intracellular fate of DOX administered as free drug compared with FTn/FTn–PEG$_{2k}$/DOX in 3LL cells. Free DOX primarily localized in the cell nuclei 2 h after its addition to cells, whereas FTn/FTn–PEG$_{2k}$/DOX were observed in both the cytoplasm and nucleus (Fig. 5 E and F). Image-based quantification revealed that, compared with nucleus, ∼95% and 55% of DOX delivered via FTn/FTn–PEG$_{2k}$ were found in cytoplasm 30 min and 2 h after adding FTn/FTn–PEG$_{2k}$/DOX to the cells (Fig. 5F). The findings here collectively suggest that free DOX are taken up by cells by passive diffusion through the cell membrane (33), whereas FTn/FTn–PEG$_{2k}$/DOX are endocytosed, release DOX in lysosomes, and subsequently the released drug molecules diffuse into cell nuclei.

Penetration of FTn/FTn–PEG$_{2k}$/DOX Within Multicellular Tumor Spheroids. FTn/FTn–PEG$_{2k}$/DOX or free DOX in aqueous solution at an identical DOX concentration were incubated with 3LL-based tumor spheroids to compare in vitro tumor penetration. 3D-reconstucted confocal images of the spheroids showed that free DOX

Fig. 6. Improved therapeutic efficacy provided by locally administered FTn/FTn–PEG$_{2k}$/DOX in an orthotopic mouse model of proximal lung cancer. (A) Colocalization of FTn/FTn–PEG$_{2k}$/DOX (red) and an orthotopically established 3LL lung tumor tissue (green) at 2 h postadministration of the nanocages. Cell nuclei are stained with DAPI (blue). (Scale bar, 100 μm.) (B) Bioluminescence signal over time postinoculation through IVIS imaging. Mice were untreated or treated with intratracheally administered free DOX or FTn/FTn–PEG$_{2k}$/DOX, 3 d following the tumor inoculation (n = 10 mice per group). (C) Quantitative analysis of the bioluminescence signal over time. *P < 0.05 compared with untreated or free DOX. (D) Kaplan–Meier survival curves for the mice with and without treatment. **P < 0.01 compared with untreated or free DOX.

remained primarily at the periphery of the spheroids, whereas FTn/FTn–PEG$_{2k}$/DOX uniformly distributed throughout the entire tumor spheroid (Fig. 5G, Left). Quantification of the DOX signal in the reconstructed 3D images revealed that the mean fluorescence signal intensity of FTn/FTn–PEG$_{2k}$/DOX in the entire spheroid was significantly greater than that of free DOX (P < 0.01) (Fig. 5G, Right). Further, we confirmed with multiple middle section images of the tumor spheroids that FTn/FTn–PEG$_{2k}$/DOX exhibited a greater 2D penetration from the surface toward the center compared with free DOX (P < 0.01) (Fig. 5H). Improved penetration of FTn/FTn–PEG$_{2k}$/DOX compared with free DOX was also observed in other tumor spheroid models constructed with human lung cancer cell lines, including A549, H460, and H1975 (Fig. S7).

We next sought to determine the in vitro tumor-killing capacity of FTn/FTn–PEG$_{2k}$/DOX compared with free DOX using 3LL cells constitutively expressing luciferase. The IC$_{50}$ of DOX and FTn/FTn–PEG$_{2k}$/DOX were 0.48 and 1.1 μM, respectively (Fig. S8 A and B). Despite the higher IC$_{50}$, FTn/FTn–PEG$_{2k}$/DOX provided superior ability of delaying the growth of 3LL tumor spheroids compared with free DOX (P < 0.05) (Fig. S8 C and D), likely due to increased penetration.

In Vivo Efficacy of FTn/FTn–PEG$_{2k}$/DOX in an Orthotopic Mouse Lung Cancer Model. To establish a proximal lung cancer model, we intratracheally inoculated C57BL/6 mice with 3LL cells constitutively expressing mCherry or luciferase. Similar to our observation with FTn/FTn–PEG$_{2k}$ (Fig. 4F), intratracheally administered FTn/FTn–PEG$_{2k}$/DOX were found preferentially distributed within the orthotopically established, mCherry-expressing tumor tissue (Fig. 6A). For the antitumor efficacy study, we first confirmed with bioluminescence imaging that luciferase-expressing tumor tissues were established throughout the upper airways 3 d after the inoculation (Fig. S9). Subsequently, tumor growth was monitored over time, following a single intratracheal administration of free DOX or FTn/FTn–PEG$_{2k}$/DOX. Mice treated with FTn/FTn–PEG$_{2k}$/DOX exhibited a significant delay in tumor progression compared with mice that were either untreated or treated with free DOX (Fig. 6B). FTn/FTn–PEG$_{2k}$/DOX effectively inhibited tumor growth 11 d after treatment, as reflected by a 40-fold and 17-fold decrease in signal intensity (from the luciferase-expressing tumor cells) (P < 0.05) compared with mice that were untreated and mice that were treated with free DOX, respectively (Fig. 6C). Survival was also significantly improved for mice treated with FTn/FTn–PEG$_{2k}$/DOX compared with untreated and free DOX-treated mice (P < 0.01). The median survival for untreated mice and free DOX-treated mice was only 18 d, whereas treatment with FTn/FTn–PEG$_{2k}$/DOX resulted in a 60% progression-free survival after 60 d (Fig. 6D). Of note, intratracheal administration of blank FTn/FTn–PEG$_{2k}$ devoid of DOX had no effect on the tumor growth and survival (Fig. S10).

Discussion

In this paper, we introduce a simple two-pronged delivery system based on a naturally occurring human protein and FDA-approved PEG molecules that overcomes multiple major delivery barriers. Unlike conventional PEGylation methods that often compromise intrinsic functionalities of core protein (24), our "hybrid" strategy does not affect the inherent ability of FTn to selectively interact with, and internalize into, cancer cells. This FTn/FTn–PEG$_{2k}$ provides (i) widespread distribution throughout the mucus-covered lung airways in vivo, (ii) deep penetration into the cores of 3D multicellular tumor spheroids and preferential distribution within solid tumor tissue in an orthotopic lung cancer model, (iii) tumor-specific cell uptake in lung cancer cells, and (iv) intracellular drug release only after cell uptake. These unique benefits combine to provide unrivaled efficacy in an orthotopic mouse model of highly aggressive airway lung cancer, including 60% survival at day 60 with FTn/FTn–PEG$_{2k}$/DOX compared with a median survival
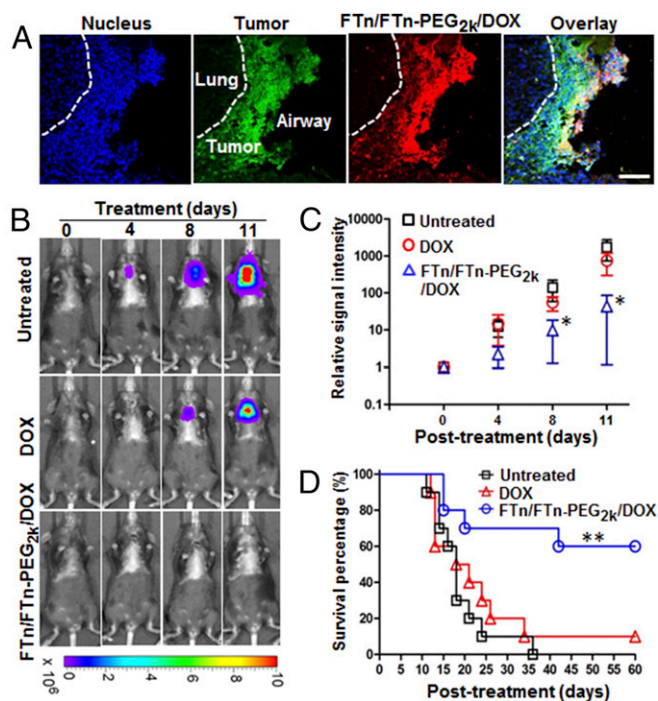
of only 18 d in animals treated with an equivalent dose of free DOX and in untreated animals. This system may offer a promising therapeutic option for treating locally confined airway lung cancers that encompass at least 40% of all lung cancer cases (34).

We have previously demonstrated that high PEG surface densities conferring brush-like coatings (i.e., [Γ/SA] ≥ 1 where [Γ] and [SA] represent total unconstrained PEG surface area and total particle surface area, respectively) (27, 35) allow nanoparticles to avoid adhesive trapping in mucus (16, 27, 36, 37) and ECM (38, 39), leading to efficient penetration through these biological barriers. We thus formulated PEGylated FTn possessing a high surface PEG density that resulted in a dense brush conformation of PEG, with [Γ/SA] of 2.2 ± 0.3. The measured surface PEG densities are comparable to those of biodegradable nanoparticles that we have previously confirmed to efficiently penetrate human cervicovaginal (27) and airway (40) mucus. The mucus-penetrating property of PEGylated FTn was confirmed by their uniform and widespread distribution throughout the mucus-covered rodent airways in vivo. In contrast, non-PEGylated FTn was found aggregated and sparsely distributed in the airways. Further, a greater amount of FTn/FTn–PEG$_{2k}$ compared with FTn was retained in the lung airways, in agreement with our pervious observation with polymer-based DNA nanoparticles possessing a similar PEG surface coating (29). Inhaled nanoparticles that efficiently penetrate the mucus gel layer are cleared more slowly by the MCC mechanism from the lung airways (16, 29). The ability to remain in the airways longer, achieve more uniform distribution within the airways, penetrate the mucus gel barrier to reach the underlying cells, and yet still be preferentially taken up by tumor cells via a specific receptor, TfR 1, is a unique benefit of the described delivery systems, and FTn with a dense coating with 2 kDa PEG (i.e., FTn/FTn–PEG$_{2k}$) were the best in this regard.

The FTn/FTn–PEG$_{2k}$ efficiently penetrated tumor tissue in vitro (i.e., human and rodent lung cancer cell-based 3D tumor spheroids) and in vivo, which is essential for widespread chemotherapeutic delivery throughout the tumor and, thus, therapeutically effective chemotherapy (32, 41). This result is in good agreement with previous reports demonstrating widespread dispersion of small PEGylated particles within tumor tissues (42, 43). However, we found that non-PEGylated FTn were capable of distributing throughout the entire tumor as effectively as the FTn/FTn–PEG$_{2k}$. In contrast, FTn PEGylated with higher MW PEG were unable to efficiently penetrate tumor tissue. Interestingly, we found that tumor penetration of FTn/FTn–PEG$_{2k}$ required specific interactions between the FTn and TfR 1, similar to the mechanism by which FTn/FTn–PEG$_{2k}$ were taken up by cancer cells. These results altogether suggest that efficient tumor penetration by FTn/FTn–PEG$_{2k}$ may occur via TfR 1-dependent transcytosis, although the involvement of simple diffusion through the extracellular space within the tumor microenvironment cannot be fully excluded.

All previous studies that investigated FTn as a delivery platform used methods of encapsulating payloads (10–12, 44). Here, we chose to conjugate DOX to the FTn to improve the drug loading efficiency and avoid drug release before uptake by cancer cells. Specifically, DOX molecules were conjugated to FTn/FTn–PEG$_{2k}$ via acid-labile linkers; these linkers are stable at extracellular-neutral or near-neutral pH but readily degrade at endolysosomal acidic pH (45). It should be noted that the tumor microenvironment can be slightly acidic (pH 6.5–6.8) (46), but the specific linker used in this study requires substantially lower pH (<6.0) to be degraded (47). We confirmed that DOX molecules were released at pH 5.0 while being stably associated with FTn/FTn–PEG$_{2k}$ at pH 7 and were found both in the cytoplasm and nucleus of lung cancer cells in vitro. In contrast, carrier-free DOX was found only in the nucleus. These findings suggest that FTn/FTn–PEG$_{2k}$, following TfR 1-dependent endocytosis (7, 8), may facilitate timely release of DOX in intracellular acidic vesicles. It is important to note that this loading strategy allows "tumor-penetrating" FTn/FTn–PEG$_{2k}$ to carry stably loaded DOX deep into the tumor cores, thus providing significantly improved drug distribution throughout the tumor tissue compared with free DOX that would enter every cell that it encounters in the airways.

Materials and Methods

Reassembly and Characterization of Hybrid FTn. Typically, FTn and conjugated FTn were mixed at designated molar ratios in PBS (pH 7.4) at a final nanocage concentration of 0.4 μM and were disassembled to subunits by adjusting pH to 2. Following a 20-min incubation, pH was tuned back to 7.0–7.4. The mixture was incubated overnight for the reassembly to yield hybrid FTn. Based on an optimization process to identify an ideal ratio, PEGylated FTn (i.e., FTn/FTn–PEG$_x$) were formulated with 50% of FTn–PEG$_x$s in all studies. For the fluorescent labeling of PEGyalted FTn, half of the non-PEGylated FTn were replaced with fluorescently labeled FTn (i.e., 25% each for FTn and fluorescently labeled FTn).

HDs of FTn and disassembled FTn were analyzed by size exclusion chromatography equipped with a Superose 6 column following previous reports (48, 49). Briefly, the protein standards with known HDs (Bio-Rad), including M1 (thyroglobulin: 669 kDa, 18.8 nm HD), M2 (γ-globulin: 158 kDa, 11.9 nm HD), M3 (ovalbumin: 44 kDa, 6.13 nm HD), M4 (myoglobin: 17 kDa, 3.83 nm HD), and M5 (vitamin B$_{12}$: 1.35 kDa, 1.48 nm HD), were analyzed using gel-filtration chromatography (GFC), and subsequently a standard curve of HD vs. retention time was established. The HDs of FTn at pH 7.4 and pH 2.0 were calculated to be 13.2 and 1.8–5.4 nm, respectively (Fig. S1).

The hybrid FTn were also characterized by gel electrophoresis. To enable the detection of signal from the gel by UV light excitation, AF488-labeled hybrid FTn were used for this study. The labeled FTn were analyzed following electrophoresis in an agarose gel by electrophoresis.

To assess the PEG surface density on FTn/FTn–PEG$_{2k}$, hybrid nanocages were formulated with FTn and FITC-labeled FTn–PEG$_{2k}$s. The number of PEG chains per FTn/FTn–PEG$_{2k}$ was fluorometrically determined to be 107 ± 13. Subsequently, the PEG surface density ([Γ]) was calculated to be ∼0.24 ± 0.03 PEG$_{2k}$ per square nanometer by the following formula, where D is the average diameter of FTn/FTn–PEG$_{2k}$:

$$[\Gamma] = \text{PEG molecules} \Big/ \Big[4\pi(D/2)^2\Big].$$

The ratio [Γ/SA] of total unconstrained PEG surface coverage area [Γ] to total particle surface area [SA] determines the surface PEG conformation: low-density mushroom and high-density brush regimes when [Γ/SA] < 1 and [Γ/SA] ≥ 1, respectively (27, 35). Briefly, the surface area occupied by one PEG chain was calculated by random-walk statistics and given by a sphere of diameter ξ:

$$\xi = 0.76 m^{1/2}\ [\text{Å}],$$

where m is MW of PEG chain, and the surface area occupied by one PEG molecule can be determined by $\pi(\xi/2)^2$. Thus, the [Γ/SA] ratio is 2.2 ± 0.3, which falls in the dense brush regime.

In Vivo Distribution of FTn Formulations Throughout the Mouse Trachea. All animals were handled in accordance with the policies and guidelines of the Johns Hopkins University Animal Care and Use Committee, which approved the experiments. Female CF-1 mice (6–8 wk) were anesthetized under continuous flow of isoflurane (2% in oxygen). A 50-μL solution of Cy5-labeled FTn (5 μM) without and with PEG modification was administered to the lung via intranasal instillation. Ten minutes after administration, mice were killed and the entire lungs (including trachea) were removed and frozen in Tissue-Tek optimal cutting temperature compound (Sakura Finetek). Tracheas were sectioned on a Leica Cryostat (Leica Biosystems) with a section thickness of 10 μm. The sections were stained with Prolong Gold antifade with DAPI (Life Technologies), and fluorescence images of the sections were obtained using a Zeiss confocal microscope. To quantify the particle distribution, the acquired images were analyzed by following an image-based analysis method that we have previously reported (28). Briefly, at least 10 fluorescence images at 10× magnification were taken of the lungs harvested from individual animals. The images were quantified with ImageJ software. An average coverage and total particles in airways were determined for each mouse, and then these values were averaged over a group of n = 4 mice.

In Vivo Anticancer Efficacy Study. To evaluate the efficacy of FTn/FTn–PEG$_{2k}$/DOX for treating lung cancer in the airways, we established an aggressive

Huang et al.

www.manaraa.com

orthotopic mouse model of proximal lung cancer in inbred mice with intact host immunity. The model was established via intratracheal intubation of cancer cells into the tracheal and bronchial epithelium of lung airways (50), which is relevant to SCLC and squamous cell lung cancer. Briefly, female C57BL/6 mice (6–8 wk) were inoculated with 2.5×10^4 3LL-Luc cells in 50 μL of DMEM via intratracheal intubation using a 22G×1-inch Safelet catheter (Exel International). Three days after the inoculation, bioluminescence signal in the lung was observed using a Xenogen IVIS Spectrum optical imaging system. Subsequently, mice ($n = 10$ per group) were treated with a single dose of DOX or FTn/FTn–PEG$_{2k}$/DOX (0.25 mg/kg, 50 μL) administered intratracheally via a microsprayer. The tumor growth was monitored at various time points using an IVIS imaging system, and the bioluminescence signal in

the lungs at different time points was quantitatively analyzed by the Living Image (Caliper Life Sciences) software. The survival of mice was recorded daily, and data were analyzed by Kaplan–Meier survival curve. The mice were monitored by following the timeline as shown in Fig. S9.

Other detailed materials and methods are provided in *SI Materials and Methods*.

1. Shi J, Kantoff PW, Wooster R, Farokhzad OC (2017) Cancer nanomedicine: Progress, challenges and opportunities. *Nat Rev Cancer* 17:20–37.
2. Theil EC (2011) Ferritin protein nanocages use ion channels, catalytic sites, and nucleation channels to manage iron/oxygen chemistry. *Curr Opin Chem Biol* 15:304–311.
3. Lin X, et al. (2011) Chimeric ferritin nanocages for multiple function loading and multimodal imaging. *Nano Lett* 11:814–819.
4. Huard DJ, Kane KM, Tezcan FA (2013) Re-engineering protein interfaces yields copper-inducible ferritin cage assembly. *Nat Chem Biol* 9:169–176.
5. Barua S, Mitragotri S (2014) Challenges associated with penetration of nanoparticles across cell and tissue barriers: A review of current status and future prospects. *Nano Today* 9:223–243.
6. Cabral H, et al. (2011) Accumulation of sub-100 nm polymeric micelles in poorly permeable tumours depends on size. *Nat Nanotechnol* 6:815–823.
7. Li L, et al. (2010) Binding and uptake of H-ferritin are mediated by human transferrin receptor-1. *Proc Natl Acad Sci USA* 107:3505–3510.
8. Fan K, et al. (2012) Magnetoferritin nanoparticles for targeting and visualizing tumour tissues. *Nat Nanotechnol* 7:459–464.
9. Kukulj S, et al. (2010) Altered iron metabolism, inflammation, transferrin receptors, and ferritin expression in non-small-cell lung cancer. *Med Oncol* 27:268–277.
10. Liang M, et al. (2014) H-ferritin-nanocaged doxorubicin nanoparticles specifically target and kill tumors with a single-dose injection. *Proc Natl Acad Sci USA* 111:14900–14905.
11. Zhen Z, et al. (2013) RGD-modified apoferritin nanoparticles for efficient drug delivery to tumors. *ACS Nano* 7:4830–4837.
12. Zhen Z, et al. (2013) Ferritin nanocages to encapsulate and deliver photosensitizers for efficient photodynamic therapy against cancer. *ACS Nano* 7:6988–6996.
13. Dong HY, Wilkes S, Yang H (2011) CD71 is selectively and ubiquitously expressed at high levels in erythroid precursors of all maturation stages: A comparative immunochemical study with glycophorin A and hemoglobin A. *Am J Surg Pathol* 35:723–732.
14. Ponka P, Lok CN (1999) The transferrin receptor: Role in health and disease. *Int J Biochem Cell Biol* 31:1111–1137.
15. Kim N, Duncan GA, Hanes J, Suk JS (2016) Barriers to inhaled gene therapy of obstructive lung diseases: A review. *J Control Release* 28:465–488.
16. Suk JS, Xu Q, Kim N, Hanes J, Ensign LM (2016) PEGylation as a strategy for improving nanoparticle-based drug and gene delivery. *Adv Drug Deliv Rev* 99:28–51.
17. Schuster BS, Ensign LM, Allan DB, Suk JS, Hanes J (2015) Particle tracking in drug and gene delivery research: State-of-the-art applications and methods. *Adv Drug Deliv Rev* 91:70–91.
18. Lai SK, Wang YY, Hanes J (2009) Mucus-penetrating nanoparticles for drug and gene delivery to mucosal tissues. *Adv Drug Deliv Rev* 61:158–171.
19. Lai SK, et al. (2007) Rapid transport of large polymeric nanoparticles in fresh undiluted human mucus. *Proc Natl Acad Sci USA* 104:1482–1487.
20. Tang BC, et al. (2009) Biodegradable polymer nanoparticles that rapidly penetrate the human mucus barrier. *Proc Natl Acad Sci USA* 106:19268–19273.
21. Ensign LM, et al. (2012) Mucus-penetrating nanoparticles for vaginal drug delivery protect against herpes simplex virus. *Sci Transl Med* 4:138ra79.
22. Yang M, et al. (2011) Biodegradable nanoparticles composed entirely of safe materials that rapidly penetrate human mucus. *Angew Chem Int Ed Engl* 50:2597–2600.
23. Suk JS, et al. (2009) The penetration of fresh undiluted sputum expectorated by cystic fibrosis patients by non-adhesive polymer nanoparticles. *Biomaterials* 30:2591–2597.
24. Harris JM, Chess RB (2003) Effect of pegylation on pharmaceuticals. *Nat Rev Drug Discov* 2:214–221.
25. Zhang C, Desai R, Perez-Luna V, Karuri N (2014) PEGylation of lysine residues improves the proteolytic stability of fibronectin while retaining biological activity. *Biotechnol J* 9:1033–1043.
26. Shaunak S, et al. (2006) Site-specific PEGylation of native disulfide bonds in therapeutic proteins. *Nat Chem Biol* 2:312–313.
27. Xu Q, et al. (2015) Impact of surface polyethylene glycol (PEG) density on biodegradable nanoparticle transport in mucus ex vivo and distribution in vivo. *ACS Nano* 9:9217–9227.
28. Mastorakos P, et al. (2015) Highly compacted biodegradable DNA nanoparticles capable of overcoming the mucus barrier for inhaled lung gene therapy. *Proc Natl Acad Sci USA* 112:8720–8725.
29. Suk JS, et al. (2014) Lung gene therapy with highly compacted DNA nanoparticles that overcome the mucus barrier. *J Control Release* 178C:8–17.
30. Lee GY, Kenny PA, Lee EH, Bissell MJ (2007) Three-dimensional culture models of normal and malignant breast epithelial cells. *Nat Methods* 4:359–365.
31. Abbott A (2003) Cell culture: Biology's new dimension. *Nature* 424:870–872.
32. Minchinton AI, Tannock IF (2006) Drug penetration in solid tumours. *Nat Rev Cancer* 6:583–592.
33. Arora HC, et al. (2012) Nanocarriers enhance Doxorubicin uptake in drug-resistant ovarian cancer cells. *Cancer Res* 72:769–778.
34. Herbst RS, Heymach JV, Lippman SM (2008) Lung cancer. *N Engl J Med* 359:1367–1380.
35. Auguste DT, et al. (2006) pH triggered release of protective poly(ethylene glycol)-b-polycation copolymers from liposomes. *Biomaterials* 27:2599–2608.
36. Boylan NJ, et al. (2011) Highly compacted DNA nanoparticles with low MW PEG coatings: In vitro, ex vivo and in vivo evaluation. *J Control Release* 157:72–79.
37. Xu Q, et al. (2013) Scalable method to produce biodegradable nanoparticles that rapidly penetrate human mucus. *J Control Release* 170:279–286.
38. Nance EA, et al. (2012) A dense poly(ethylene glycol) coating improves penetration of large polymeric nanoparticles within brain tissue. *Sci Transl Med* 4:149ra119.
39. Mastorakos P, et al. (2015) Highly PEGylated DNA nanoparticles provide uniform and widespread gene transfer in the brain. *Adv Healthc Mater* 4:1023–1033.
40. Schneider CS, et al. (2017) Nanoparticles that do not adhere to mucus provide uniform and long-lasting drug delivery to airways following inhalation. *Sci Adv* 3:e1601556.
41. Sugahara KN, et al. (2010) Coadministration of a tumor-penetrating peptide enhances the efficacy of cancer drugs. *Science* 328:1031–1035.
42. Chauhan VP, et al. (2012) Normalization of tumour blood vessels improves the delivery of nanomedicines in a size-dependent manner. *Nat Nanotechnol* 7:383–388.
43. Nance E, et al. (2014) Brain-penetrating nanoparticles improve paclitaxel efficacy in malignant glioma following local administration. *ACS Nano* 8:10655–10664.
44. Zhen Z, et al. (2014) Tumor vasculature targeted photodynamic therapy for enhanced delivery of nanoparticles. *ACS Nano* 8:6004–6013.
45. Yang HM, Reisfeld RA (1988) Doxorubicin conjugated with a monoclonal antibody directed to a human melanoma-associated proteoglycan suppresses the growth of established tumor xenografts in nude mice. *Proc Natl Acad Sci USA* 85:1189–1193.
46. Wang Y, et al. (2014) A nanoparticle-based strategy for the imaging of a broad range of tumours by nonlinear amplification of microenvironment signals. *Nat Mater* 13:204–212.
47. Zhu S, et al. (2011) RGD-modified PEG-PAMAM-DOX conjugate: In vitro and in vivo targeting to both tumor neovascular endothelial cells and tumor cells. *Adv Mater* 23:H84–H89.
48. Choi HS, et al. (2010) Design considerations for tumour-targeted nanoparticles. *Nat Nanotechnol* 5:42–47.
49. Huang X, et al. (2013) Effect of injection routes on the biodistribution, clearance, and tumor uptake of carbon dots. *ACS Nano* 7:5684–5693.
50. DuPage M, Dooley AL, Jacks T (2009) Conditional mouse lung cancer models using adenoviral or lentiviral delivery of Cre recombinase. *Nat Protoc* 4:1064–1072.
51. Friedrich J, Seidel C, Ebner R, Kunz-Schughart LA (2009) Spheroid-based drug screen: considerations and practical approach. *Nat Protoc* 4:309–324.

www.manaraa.com